

Horizontal Emittance Reduction on a Synchrotron Radiation Light Source with a Robinson Wiggler

H. Abualrob,* P. Brunelle, M.-E. Couprie, M. Labat, A. Nadji, L. S. Nadolski, and O. Marcouille
Synchrotron SOLEIL, L'Orme des Merisiers, Gif-sur-Yvette, France
 (Dated: June 26, 2018)

The performance of synchrotron light facilities are strongly influenced by the photon beam brightness, that can be further increased by reducing the beam emittance. A Robinson Wiggler can be installed in a non-zero dispersion straight section to reduce the horizontal beam emittance. It is composed of an array of magnets of alternated polarities, whose both magnetic field and gradient are of opposite signs. It provides a compact solution to reduce by 50% the horizontal emittance. However, it increases the energy spread by 40%. The concept of the Robinson Wiggler (RW) is described here, the first experimental observation of the Robinson effect in a synchrotron light source on the transverse and longitudinal beam properties by the means of four existing undulators is presented and the impact on the photon flux density is studied.

INTRODUCTION

High brightness light sources have allowed for the development or the improvement of new techniques [1, 2], e.g. coherent X-ray diffraction imaging [3] and holography [4]. The brightness B is the phase-space density of the photon flux F (number of photons emitted per second per 0.1% bandwidth), evaluated in the forward direction and at the center of the source [5]: $B = \frac{d^4 F}{d\theta d\psi dx dz}$, with θ and ψ the horizontal and vertical angles, x and z the horizontal and vertical coordinates respectively. Assuming Gaussian photon distribution, and neglecting the variation of the electron transverse position due to the oscillations through the insertion device, the brightness can be written as [6]:

$$B = \frac{F}{4\pi^2 \Sigma_x \Sigma_{x'} \Sigma_z \Sigma_{z'}}$$

with $\Sigma_{x,z}$ ($\Sigma_{x',z'}$) the size and (the divergence) of the photon beam resulting from the convolution of the electron beam size (divergence) with the photon emission of a single electron. The beam size and divergence can be expressed as: $\Sigma_{x,z} = \sqrt{\sigma_{x,z}^2(e^-) + \sigma_{x,z}^2(\text{photon})}$ and $\Sigma_{x',z'} = \sqrt{\sigma_{x',z'}^2(e^-) + \sigma_{x',z'}^2(\text{photon})}$, where $\sigma_{x',z'}(\text{photon}) = \sqrt{\frac{\lambda}{2L}}$ the photon beam divergence resulting from single electron emission through an insertion device, $\sigma_{x,z}(\text{photon}) = \frac{\sqrt{2\lambda L}}{2\pi}$ the photon beam size [7], λ the wavelength of the emitted radiation and L is the length of the device.

In a non-zero dispersion straight section for a Gaussian electron beam distribution, the total horizontal beam size σ_x and divergence $\sigma_{x'}$ include contributions from both the betatron and the energy spread σ_e :

$$\begin{aligned} \sigma_x &= \sqrt{\epsilon_x \beta_x + (\eta_x \sigma_e)^2} \\ \sigma_{x'} &= \sqrt{\frac{\epsilon_x}{\beta_x} + (\eta'_x \sigma_e)^2} \end{aligned} \quad (1)$$

with ϵ_x the horizontal emittance, β_x the horizontal betatron amplitude function, η_x and η'_x the horizontal dispersion function and its derivative respectively. In the vertical plane, if the vertical dispersion function η_z and its derivative η'_z are zero, the vertical beam size σ_z and divergence $\sigma_{z'}$ are expressed as:

$$\begin{aligned} \sigma_z &= \sqrt{\epsilon_z \beta_z} \\ \sigma_{z'} &= \sqrt{\frac{\epsilon_z}{\beta_z}} \end{aligned} \quad (2)$$

with ϵ_z the vertical emittance and β_z the vertical betatron amplitude function.

At a given wavelength λ , the emittance of the photon beam ϵ_{ph} at the diffraction limit is defined by :

$$\epsilon_{ph} = \sigma_{x,z(\text{photon})} \cdot \sigma_{x',z'(\text{photon})} = \frac{\lambda}{4\pi}$$

To reach the diffraction limit, the electron beam emittance $\epsilon_{x,z}$ should satisfy the condition: $\epsilon_{x,z} \leq \frac{\lambda}{4\pi}$. For an operation at $\lambda = 1$ Angstrom, an electron beam emittance of lower than 10 pm.rad in both planes is required. Besides, the orientation of the phase space ellipse of the electron beam should match that of the photon beam emitted by a single electron.

In third generation synchrotron light sources the electron beam emittance (e.g. 3.9 nm.rad at SOLEIL [8], 2.7 nm.rad at Diamond [9]), leads to partial transverse coherence in the X-ray range. Recently, diffraction limited storage rings have appeared [10, 11]. Indeed, different approaches are implemented to further reduce the emittance of existing light sources.

The natural horizontal emittance ϵ_{x0} at equilibrium between quantum excitation and radiation damping for an isomagnetic lattice is [12, 13]:

$$\epsilon_{x0} = \frac{1}{J_x} \frac{\oint \frac{H_x(s)}{\rho} ds}{\oint \frac{1}{\rho^2} ds} \quad (3)$$

with ρ is the radius of curvature and $H_x(s)$ is the dispersion invariant given by [13]:

$$H_x(s) = \gamma_x \eta_x^2(s) + 2\alpha_x \eta_x(s) \eta'_x(s) + \beta_x \eta'_x{}^2(s)$$

* hadil.abualrob@najah.edu; Also at An-Najah National University, Nablus, Palestine

where γ_x , β_x and α_x are Twiss parameters [14]. The natural horizontal emittance ϵ_{x0} for an isomagnetic lattice can be rewritten in the simplified form as [15]:

$$\epsilon_{x0} = F(\text{lattice}) \frac{E^2}{N^3} \quad (4)$$

where $F(\text{lattice})$ is a constant that depends on the lattice design, N is the number of identical dipoles in the storage ring.

A first approach for reducing the horizontal emittance is given by increasing the number of dipoles in the storage ring, moving from Double Bend Achromat lattice (DBA) [16] (two dipole magnets with focusing quadrupoles between them to form an achromatic cell) and Triple Bend Achromat (TBA) [16] (combination of a DBA with a dipole at the center) to Multiple Bend Achromat (MBA) lattice [17]. Among others, there are several examples: MAX IV operating with 7-BA lattice and transverse gradient in the dipoles produces a beam with horizontal emittance of 250 pm.rad [18–20], the project of SPring-8 upgrade, first based on a 10-BA [21] and later on a 5-BA [22] to achieve a horizontal emittance of 150 pm.rad, the ESRF upgrade proposing a new design based on 7-BA lattice to reach a horizontal emittance of 150 pm.rad [23, 24], etc. After the shutdown of the Tevatron collider, it is proposed to use its large tunnel (6.28 km circumference) to house a storage ring of a new light source called the Tevatron-Sized Ultimate Storage Ring (TeVUSR) [25], that thanks to this large circumference, expects a horizontal emittance of 4 pm.rad using a 7-BA lattice.

A second approach for horizontal emittance reduction consists in increasing the damping rate by installing damping wigglers in zero dispersion straight sections [13] to enhance the radiation damping by contributing to the synchrotron integrals. One can introduce the ratio $F_w = \frac{I_{2w}}{I_{2a}}$ where I_{2a} is the second synchrotron integral without the wiggler and I_{2w} is the additive term due to the wiggler [26]. The total horizontal emittance with the damping wiggler can be written as:

$$\epsilon_x = \epsilon_{xa} \frac{J_{x0}}{J_{x0} + F_w} + \epsilon_{xw} \frac{F_w}{J_{x0} + F_w} \quad (5)$$

where ϵ_{xa} and J_{x0} are the emittance and the damping partition number produced in the absence of wiggler, respectively. ϵ_{xw} is the emittance generated by the wiggler in the limit of $F_w \rightarrow \infty$. The required wiggler length L_w for an isomagnetic lattice is given by:

$$L_w = \frac{6C(B\rho)^2}{r_e c \tau_z \gamma^3 B_w^2} \frac{F_w}{1 + F_w} \quad (6)$$

with C the machine circumference, $B\rho$ the magnetic rigidity, r_e the classical electron radius, c the speed of light in vacuum, τ_z the damping time, γ the relativistic factor, B_w the wiggler field. Different light sources adopted this solution among which PETRA III [27] that

reached a horizontal emittance of 1 nm.rad by installing 80 m long damping wigglers, PEP-X that replaced the PEP-II tunnel and reached a horizontal emittance of 0.14 nm.rad by installing 90 m of damping wigglers [13], NSLS II at Brookhaven National Laboratory installed 21 m of damping wigglers in order to achieve 1 nm.rad horizontal emittance [28].

The two strategies, i.e. adding damping wigglers and increasing the number of dipoles to low emittance lattices, can also be combined. In this respect, an "ultimate" PEP-X lattice has been proposed based on 7-BA lattice together with a 90 m damping wigglers in one of the straight sections to reduce the horizontal emittance to 11 pm.rad [29] at zero current. However, the drawbacks of the damping wigglers solution is the requirement of long insertion devices and the energy consumption of the RF system.

A third approach to reduce the horizontal emittance is given by adjusting the damping partition number by installing in a non-zero dispersion straight section a Robinson wiggler (RW) [30], i.e. a magnetic system of high field transverse gradient superimposed to its main alternated pole wiggler field. It consists in installing a magnetic system producing a periodic vertical magnetic field B_z and transverse field gradient dB_z/dx . It is enough to install this wiggler in non-zero dispersion straight section without any need to modify the existing infrastructure. First observations have been carried out with success at Cambridge Electron Accelerator [31], and in the PS at CERN [32] showing 50% horizontal emittance reduction. RW has been recently adopted by other light sources to reduce the horizontal emittance like Heifei Light Source [33], Shanghai Synchrotron Radiation Facility [34] and the Metrology Light Source that benefited from RW to improve Touschek lifetime by lengthening the bunch [35, 36].

In this paper, we show that the Robinson wiggler approach applied to the case of the SOLEIL storage ring enables the reduction of the horizontal emittance, while increasing the energy spread. The experiment has been performed using four U20 undulators as a RW-like by creating off-axis displacement of the electron beam horizontally and simultaneously in the four undulators for getting the required field gradient product. Effects on the radiation are also derived.

I. THEORETICAL APPROACH: HORIZONTAL EMITTANCE REDUCTION BY DAMPING PARTITION NUMBER ADJUSTMENT

A. Transverse and longitudinal properties

Over one turn in the storage ring, the electron loses energy by emitting radiation, and gains energy from the RF system. Assuming a sinusoidal RF voltage, the electron motion behaves as a damped harmonic oscillator [12]. The damping process is characterized by the so-

called damping partition D that determines the damping rate of the emitted radiation. Considering a storage ring of equilibrium horizontal emittance ϵ_{x0} , the variation of the horizontal emittance ϵ_x due to the modification of the damping partition D at equilibrium between quantum excitation and radiation damping can be expressed as [37]:

$$\epsilon_x = \epsilon_{x0} \frac{1}{1 - D} \quad (7)$$

The damping partition numbers J_x , J_z , J_s , characterizing the damping rate, are defined as [12]:

$$J_x = 1 - D, \quad J_z = 1, \quad J_s = 2 + D$$

According to Robinson theorem [30], the total sum of damping partition numbers i.e. of the amount of damping decrement over all degrees of freedom is constant: $\sum J_i = J_x + J_z + J_s = 4$. In terms of the synchrotron integrals I_2 and I_4 , J_x is expressed as $J_x = 1 - (I_4)/(I_2)$ [12], where I_2 and I_4 are given by:

$$\begin{cases} I_2 = \oint \frac{1}{\rho^2} ds \\ I_4 = \oint \frac{\eta_x(s)}{\rho} \left(\frac{1}{\rho^2} - 2K(s) \right) ds \end{cases}$$

where $K(s)$ is the normalized focusing strength in the dipole. It is given in terms of the dipole field B_z and its transverse variation dB_z/dx (usually known as the field gradient) as $K(s) = (1)/(B_z \rho)(dB_z/dx)$.

At equilibrium between quantum excitation and radiation damping, the relative energy spread for an isomagnetic lattice is [12]:

$$\sigma_e^2 = \frac{C_q \gamma^2}{J_s \rho} \quad (8)$$

The variation of the energy spread σ_e as a function of D can be written as follows [37]:

$$\sigma_e^2 = \sigma_{e0}^2 \frac{2}{2 + D} \quad (9)$$

According to equations 7 and 9, the horizontal emittance ϵ_x and the relative energy spread σ_e can be modified by varying the horizontal and the longitudinal damping partition numbers J_x and J_s respectively; i.e. by varying the damping partition D . The damping partition for a given lattice is determined by its design. It is given in terms of the magnetic field B_z and the field gradient dB_z/dx by:

$$D = \frac{\frac{1}{2\pi} \left(\oint \frac{\eta_x}{\rho^3} ds + \frac{2}{B^2 \rho^2} \oint \eta_x B_z \frac{dB_z}{dx} ds \right)}{\oint \frac{ds}{\rho^2}} \quad (10)$$

For an isomagnetic storage ring with identical bending magnets, and equipped with separate function magnets

(i.e. bending magnets for deflection and quadrupoles for focusing) such as SOLEIL, the damping partition is given by:

$$D = \frac{\alpha R}{\rho}$$

where R is the radius of the storage ring and α is the momentum compaction factor. For the case of SOLEIL ($\alpha = 4.16 \times 10^{-4}$, $R = 57.37$ m, $\rho = 5.3$ m), the damping partition $D \approx 0$.

If D can be reduced from its usual value $D \approx 0$ to $D = -1$, the horizontal emittance can be divided by 2 (see equation 7), while the energy spread will be increased by $\sqrt{2}$ (see equation 9).

The bunch length represents the longitudinal distribution of the electron in the phase space and is related to energy spread. In the zero current regime, the bunch length σ_t is given by [38]:

$$\sigma_t = \frac{\alpha}{2\pi f_s} \sigma_e \quad (11)$$

where f_s is the synchrotron frequency expressed in terms of the radio-frequency voltage V , the momentum compaction factor α , the harmonic number h , the electron energy E , and the revolution frequency f_0 as:

$$f_s = f_0 \sqrt{\frac{V \alpha h}{2\pi E}} \quad (12)$$

B. Requirements in terms of magnetic field

For an isomagnetic lattice, the damping partition given by equation 10 can be reduced to:

$$D = \frac{\rho \langle \eta_x \rangle_s}{\pi (B \rho)^2} \int_0^{L_w} B_z \frac{dB_z}{dx} ds \quad (13)$$

The damping partition D can be significantly modified by installing an insertion device of high vertical field and high field gradient in a non-zero dispersion straight section. A RW of length L_w and peak field B_w contributes to the modification of D if inserted in a straight section whose average dispersion function over the length of the wiggler is $\langle \eta_x \rangle$. The damping partition can get a negative value if $B_w \frac{dB_w}{dx} < 0$ according to equation 13.

The SOLEIL storage ring hosts three types of straight sections, as presented in Table I, all providing non-zero dispersion. D could be reduced from ≈ 0 to -1 by installing a wiggler of $\int B_w (dB_w/dx) ds = 193.4 T^2$ in a short straight section ($\eta_x = 0.252$ m), leading to a reduction of the horizontal emittance from its present value of 3.9 nm.rad to 1.95 nm.rad. Inversely, the energy spread will be increased from the present value of 1.01×10^{-3} to 1.43×10^{-3} .

TABLE I. Length of straight sections at SOLEIL and optical functions at the center

Straight section	Length (m)	η_x (m)	β_x (m)	β_z (m)
Long	4×12	0.206	5.58	8.03
Medium	12×7	0.165	4.6	2.24
Short	8×3.6	0.252	14.38	2.36

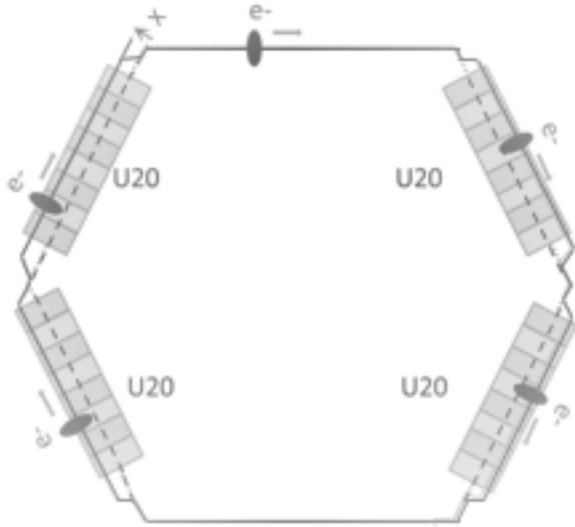


FIG. 1. Schematic presentation of the simultaneous horizontal bumps in the four U20 undulators. Dashed line: the on-axis electron beam trajectory, continuous line: the displaced trajectory by applying a horizontal bump of value x .

II. EXPERIMENTAL OBSERVATION OF THE ROBINSON EFFECT AT SOLEIL

To bring out the effect of a RW on the emittance and the relative energy spread at SOLEIL, different experiments have been performed using four already existing in-vacuum undulators (four U20s) [39, 40] in the storage ring. The four U20s are all installed in dispersive short straight sections and generate periodic vertical magnetic field and significant off-axis field gradient. To maximize the total effect, the four U20s were used simultaneously. Figure 1 shows the schematic experimental setup. The electron beam is displaced off-axis in the four undulators by applying simultaneous horizontal bumps using horizontal dipolar correctors at the entrance and at the exit of each undulator. At the entrance the electron beam is displaced horizontally parallel to its initial trajectory and comes back to the initial one at the exit of the undulator. After each horizontal simultaneous bump, the tunes are set back to the nominal values using two quadrupole families. Horizontal beam size and bunch length are measured at each bump with the four U20s open at maximum gap (bare machine) and with the four undulators closed at minimum gap of 5.5 mm.

To study the Robinson effect, the horizontal beam size and the bunch length are measured at 18 mA current

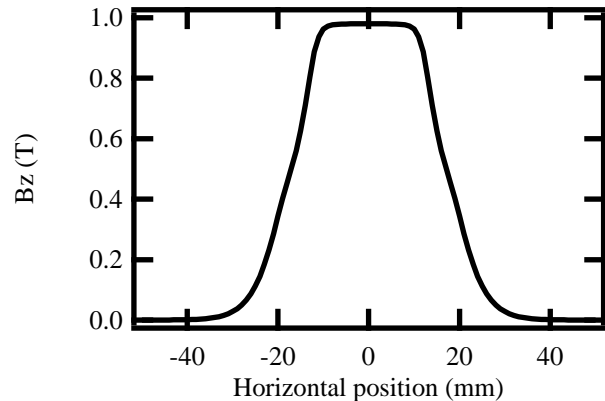


FIG. 2. Peak magnetic field of a U20 undulator calculated as a function of the horizontal beam position with RADIA for the parameters listed in Table II (minimum gap).

TABLE II. Main characteristics of the in-vacuum U20 undulators used for the experimental study of the Robinson effect

Characteristic	Value	Unit
Type	in-vacuum	-
Magnet material	$Nd_2Fe_{17}B$	-
Magnet dimensions (s, x, z)	7.5, 50, 30	mm
Magnet chamfer size	4×4	mm
Magnetization B_r	1.05	T
Pole material	Vanadium Permendur	-
Pole dimensions (s, x, z)	2.5, 33, 22	mm
Pole saturation field B_s	2.35	T
Pole chamfer size	4×4	mm
Peak field	0.97	T
Period length	20	mm
(Magnetic) minimum gap height	5.5	mm
Period number	98	-
Deflection parameter	1.8	-

distributed in 416 bunches. The low current per bunch enables operation of the machine close to the zero current regime so as to satisfy equation 11.

A. The U20: a RW-like undulator

Figure 2 illustrates the peak field variation over the horizontal range ± 50 mm for a U20 undulator calculated with RADIA code [41, 42] for the parameters given in Table II. The magnetic field of a U20 is constant over ± 10 mm in the vicinity of the central on-axis position. Beyond ± 10 mm, the peak field drops sharply creating a strong magnetic field gradient. The superimposition of the strong magnetic field to the strong field gradient as in a RW can be achieved by creating off-axis propagation of the electron beam through the U20. Consequently, a U20 undulator is a good candidate to study Robinson effect thanks to the particular transverse variation of its magnetic field over wide horizontal range.

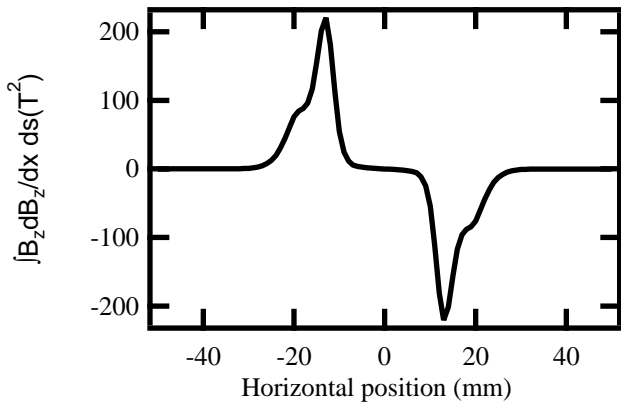


FIG. 3. Transverse variation of $\int B_z(dB_z/dx)ds$ calculated with RADIA for the four U20 undulators closed at gap 5.5 mm.

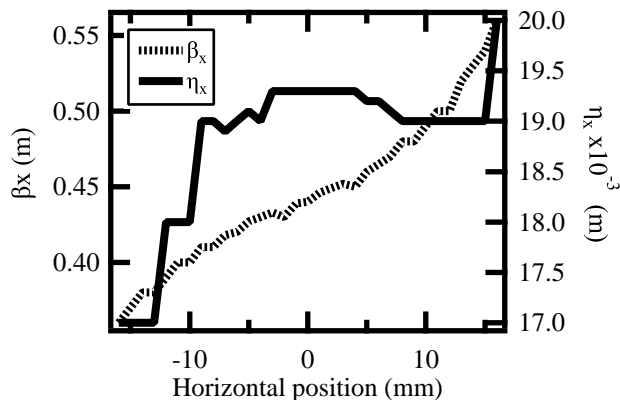


FIG. 4. Variation of the horizontal betatron and dispersion functions with the horizontal position in the four U20 undulators at the pinhole camera location. Functions obtained with AT simulation code.

Figure 3 illustrates the magnetic field multiplied by the field gradient integrated over the undulator length $\int B_z(dB_z/dx)ds$ for the four U20 undulators versus transverse position. The zone of interest for the observation of the Robinson effect is that of maximum magnetic field and maximum field gradient. The four U20 undulators show a significant $\int B_z(dB_z/dx)ds$ peak of $\pm 220 T^2$ at $x = \pm 13$ mm.

B. Machine tuning for off-axis propagation

In the case of the SOLEIL storage ring, the optical functions vary significantly when horizontal bumps reach large values, since the horizontal bump creates off-axis propagation in a large number of sextupoles leading to additional focusing. The optical functions corresponding to each bump are simulated with the Accelerator Toolbox (AT) code [43] at the location of the photon beam

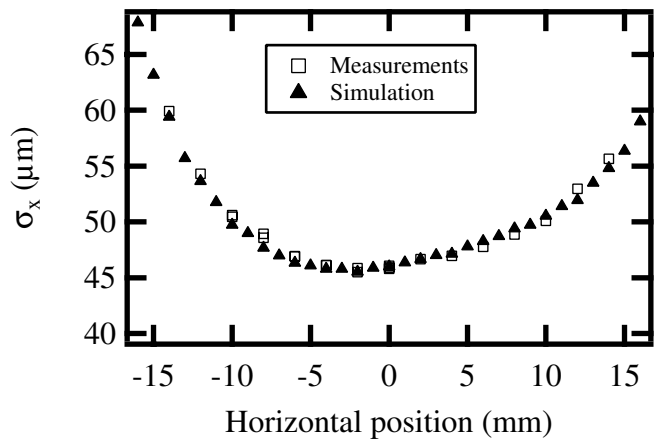


FIG. 5. Horizontal beam size variation for a bare machine as a function of the horizontal position in the four U20 undulators. \blacktriangle : orbit bump simulation with AT code, \square : measurements with the pinhole camera with a $5 \mu m$ precision.

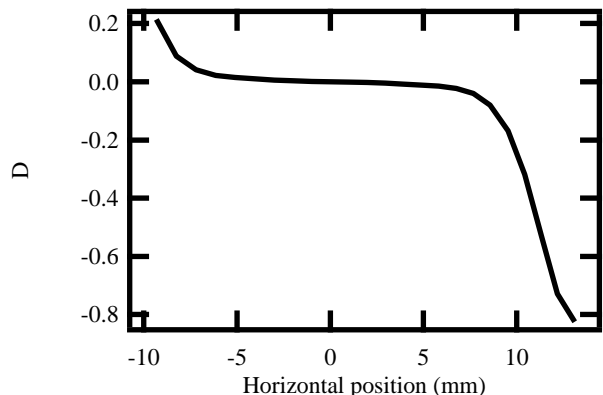


FIG. 6. Damping partition calculated with equation 13 as a function of the horizontal position when the four U20 undulators are closed at minimum gap. $\langle \eta_x \rangle$: the average horizontal dispersion function obtained by AT simulation. $B\rho$: the magnetic rigidity $B\rho = 9.13$ T.m. $\int_0^L B_z(dB_z(x)/dx) ds$: The integral of the magnetic field times the field gradient for the four U20 undulators calculated with RADIA code (see Fig. 3).

profile sensor as a function of the horizontal beam position at any given horizontal position in the four U20s and any longitudinal position in the storage ring. Figure 4 shows the AT simulation of the optical functions $\eta_x(x)$ and $\beta_x(x)$, assuming a simultaneous horizontal bump in the four U20 undulators.

Figure 5 shows the horizontal beam size measured with a pinhole camera as a function of the horizontal position for a bare machine and the beam size obtained by simulation. Good agreement between measurements and AT results confirms the good quality of the model used in AT code.

Figure 6 shows the damping partition D as a function of the horizontal position in the four U20s (undulators

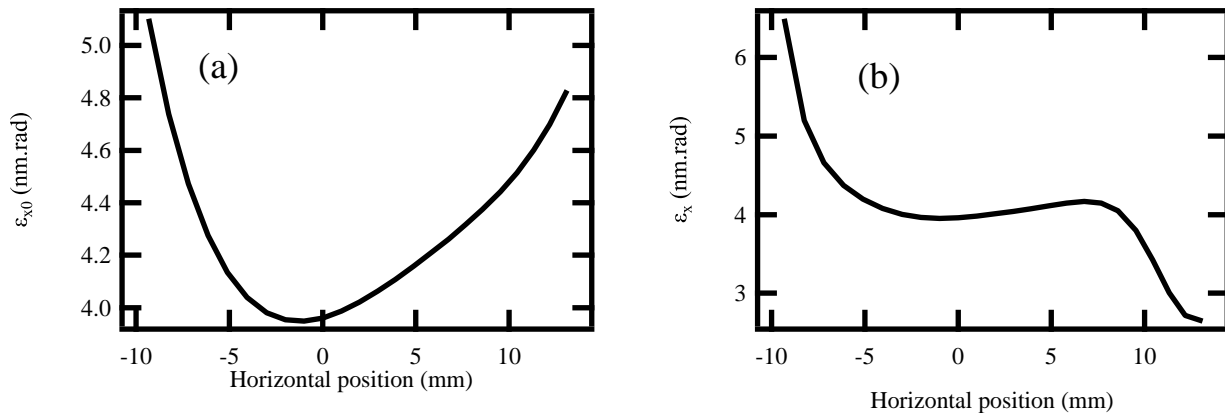


FIG. 7. (a): Natural horizontal emittance variation as a function of the horizontal beam position in the four U20 undulators obtained with AT simulation (U20s are open at maximum gap). (b): calculated horizontal emittance variation as a function of the horizontal position in the four U20 undulators (U20s are closed at minimum gap). Calculations performed with equation 7 with $\epsilon_{x0}(x)$: natural horizontal emittance corresponding to the horizontal beam position according to AT simulation and $D(x)$: the damping partition (see Fig. 6).

are closed at gap 5.5 mm) calculated with equation 13. The dissymmetry is due to the fact that $\langle \eta_x(x) \rangle$ differs for positive and negative values of the horizontal position. The damping partition can even evaluate to negative values and reaches a minimum of -0.8 , whereas a damping partition of -1 is required to reduce the horizontal emittance by factor of 2 (see equation 7). It is not possible to get the value of $D = -1$, since some beam instability appears at larger bumps leading to horizontal emittance reduction by a factor of 0.45 and energy spread increase by a factor of 1.3.

The variation of the natural horizontal emittance with the bump is also taken into account. Figure 7 (a) shows the natural horizontal beam emittance as a function of the horizontal beam position obtained with AT simulation (U20s are open). It is modified due to the horizontal beam displacement, asymmetric increase is noticed around the nominal propagation axis. Figure 7 (b) shows the calculated horizontal beam emittance with equation 7 in the case of four U20s closed at minimum gap, with the natural horizontal beam emittance $\epsilon_{x0}(x)$ deduced from Fig. 7 (a) and the damping partition $D(x)$ of Fig. 6.

C. Measurement of Robinson effect on the longitudinal beam properties

The bunch length is measured as a function of the horizontal position in the four U20s with a HAMAMATSU-C10910 Series streak camera [44] of 2 ps-FWHM resolution to infer the effect on the energy spread (equation 11). Figure 8 shows a typical bunch image detected by the streak camera. Figure 9 compares the measured bunch length with that obtained with equation 11 using the damping partition due to the four U20s closed at minimum gap found in Fig. 6. Bunch length calculations

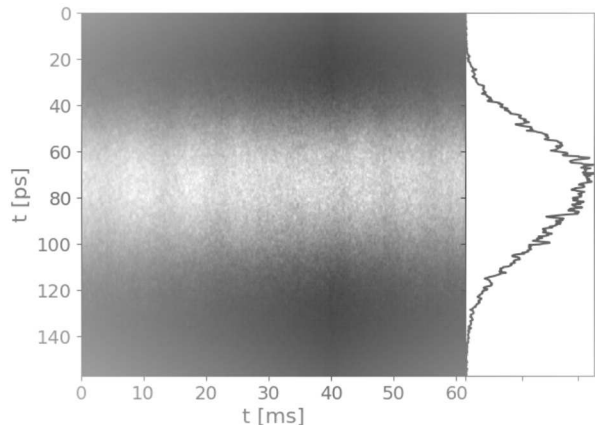


FIG. 8. Time evolution of the longitudinal bunch profile detected by streak camera. Single bunch mode, $I = 0.7$ mA, $V_{RF} = 1.37$ MV and electron beam positioned at $x = 16$ mm in the four U20s.

assumes $\alpha = 416.4 \times 10^{-6}$ to be constant as a function of the horizontal position as predicted by AT simulation, $V = 1.2$ MV, $h = 416$, $E = 2.75$ GeV, $f_0 = 847$ kHz and σ_e the energy spread calculated with equation 9 assuming constant natural energy spread ($\sigma_{e0} = 1.01 \times 10^{-3}$) over the whole horizontal range as predicted by AT simulation, and the damping partition found in Fig. 6.

Measurements confirm the expected increase of bunch length when U20s are closed at minimum gap due to the increase of the energy spread. However, measurements are less in accordance with calculations at large bump values because during the experiment it was not possible to displace the electron beam so that its horizontal position is exactly the same in the four U20s.

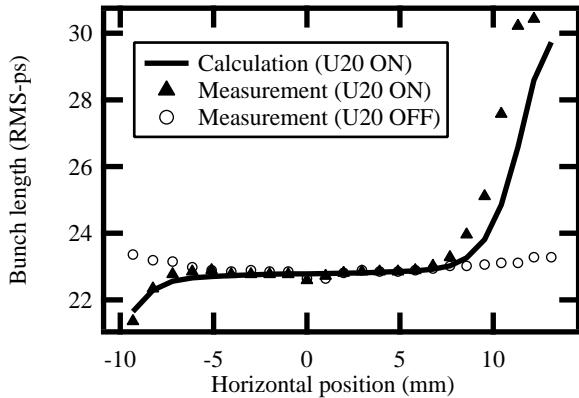


FIG. 9. Electron bunch length variation as a function of the horizontal position in the four U20 undulators. U20 ON: U20 undulators set at minimum gap (5.5 mm), U20 OFF: U20 undulators set at maximum gap (30 mm). Calculations: —, from measurements with the streak camera for the U20s set at minimum gap: \blacktriangle , at maximum gap: \circ . Streak camera of 2 ps FWHM resolution.

D. Measurement of Robinson effect on the transverse beam properties

Figure 10 shows the horizontal beam size as a function of the horizontal beam position in the four U20s measured with a pinhole camera [45] of $5 \mu\text{m}$ precision to deduce the effect on the horizontal beam emittance (equation 1), taking into account the corresponding measured energy spread and the horizontal beam size expected from theoretical calculations using equation 1, where σ_e is the calculated energy spread (see Fig. 9), η_x and β_x are the optical functions at the pinhole camera obtained with AT simulation (see Fig. 4) and ϵ_x is the horizontal beam emittance calculated with equations 7 and 13 and the optical functions η_x and β_x (see Fig. 7).

The horizontal beam size reduction due to the Robinson effect expected at $x = 12 \text{ mm}$ is confirmed by experimental observations. At large bump values, a slight shift between measurements and calculations appears because the horizontal beam position is not exactly the same in the four U20s.

III. EXPECTED SPECTRAL PERFORMANCE

Following the experimental observation of Robinson effect, the radiation properties of already installed undulators are studied under the modifications introduced by a RW with SRW (Synchrotron Radiation Workshop) code [46]. The undulator HU640 operating at low photon energy range in the linear horizontal polarization, and the U20 undulator operating at high photon energy range, are supposed to be installed in a new machine whose

emittance and energy spread are modified by a RW while

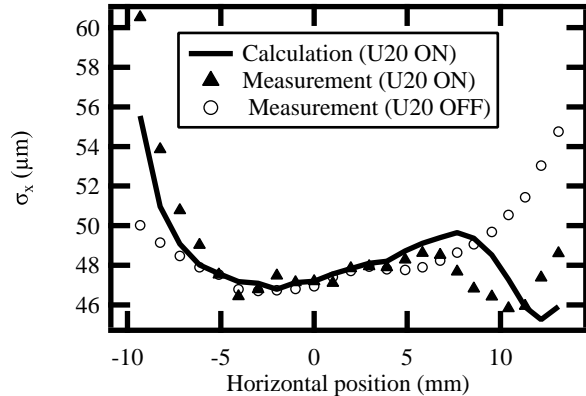


FIG. 10. Calculated and measured horizontal beam size variation at the pinhole camera as a function of the horizontal position in the four U20 undulators. U20 ON: U20 undulators set at minimum gap (5.5 mm), U20 OFF: U20 undulators set at maximum gap (30 mm). Calculations: —, measurements with the U20s set at minimum gap: \blacktriangle , at maximum gap: \circ .

assuming unperturbed dispersion and betatron functions. (see Table III for the main characteristics of both undulators).

TABLE III. Characteristics of the HU640 and U20 undulators

Undulator	HU640	U20
Technology	Electromagnetic	HPM ^a , in-vacuum
$(B_z)_{max}$	0.15 T	1.08 T
Period length	640 mm	20 mm
K	8.95	2
Energy range	(5-40) eV	(3-18) keV
Straight section	Long	Short

^a HPM: Hybrid Permanent Magnet

The effect on the spectrum can be understood by considering the various contributions of the spectral broadening $(\frac{\Delta\lambda}{\lambda})_{tot}$. For a mono-energetic filament electron beam, the undulator line presents a natural linewidth $(\frac{\Delta\lambda}{\lambda})_{hom} = \frac{0.9}{nN_0}$ with n the harmonic number and N_0 the number of the undulator periods, the inhomogeneous broadening due to the emittance $(\frac{\Delta\lambda}{\lambda})_\epsilon = \left(\frac{\gamma^2}{1+\frac{K^2}{2}}\right)(\sigma_x^2 + \sigma_z^2)$ with γ the relativistic factor and K the deflection parameter of the undulator, the inhomogeneous broadening due to the energy spread $(\frac{\Delta\lambda}{\lambda})_{\sigma_e} = 2\sigma_e$ and the inhomogeneous broadening due to the beam size $(\frac{\Delta\lambda}{\lambda})_\sigma = \left(\frac{\gamma^2}{1+\frac{K^2}{2}}\right)\left(\left(\frac{\sigma_x}{d}\right)^2 + \left(\frac{\sigma_z}{d}\right)^2\right)$ at a distance d where the radiation is collected. Consequently, the total spectral broadening can be expressed as:

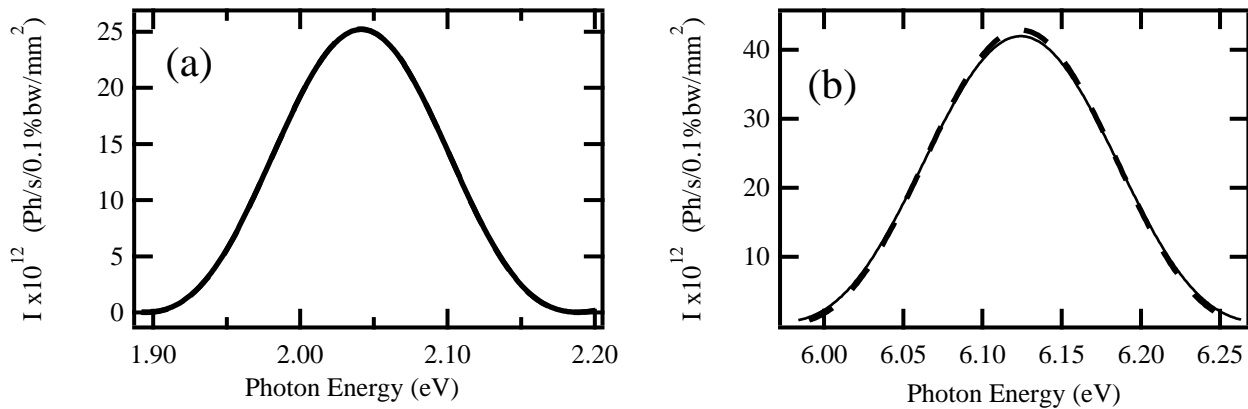


FIG. 11. Flux density emitted by the undulator HU640 ($K = 8.95$) calculated with SRW through an aperture of $0.1 \times 0.1 \text{ mm}^2$ located at 10 m from the source. (a): zoom on the harmonic H1, (b) zoom on the harmonic H3. — $\epsilon_x = 1.95 \text{ nm.rad}$, $\sigma_e = 1.428 \times 10^{-3}$. - - $\epsilon_x = 3.9 \text{ nm.rad}$, $\sigma_e = 1.01 \times 10^{-3}$. Beam energy of 2.75 GeV and beam current of 500 mA.

$$\left(\frac{\Delta\lambda}{\lambda}\right)_{tot} = \sqrt{\left(\frac{0.9}{nN_0}\right)^2 + \left(\frac{\gamma^2}{1 + \frac{K^2}{2}}\right)^2 (\sigma_{x'}^4 + \sigma_{z'}^4) + (2\sigma_e)^2 + \left(\frac{\gamma^2}{1 + \frac{K^2}{2}}\right)^2 \left(\left(\frac{\sigma_x}{d}\right)^4 + \left(\frac{\sigma_z}{d}\right)^4\right)} \quad (14)$$

Figure 11 compares the calculated flux density emitted by the HU640 undulator considering the present SOLEIL horizontal emittance and energy spread, and that modified due to the assumed presence of a RW. The flux density emitted by the HU640 for the first (H1) and the third (H3) harmonics remains practically unchanged. The harmonic H1 is unaffected whereas the H3 flux is reduced by 0.5%. The harmonic widths are mostly determined by the energy spread, since $\left(\frac{\Delta\lambda}{\lambda}\right)_{\sigma_e} \approx 2.8 \times 10^{-3}$, while $\left(\frac{\Delta\lambda}{\lambda}\right)_{\epsilon} = 4.95 \times 10^{-4}$ and $\left(\frac{\Delta\lambda}{\lambda}\right)_{\sigma} = 4.7 \times 10^{-4}$ (calculated at the source point: $\sigma_x = 257.6 \text{ }\mu\text{m}$, $\sigma_z = 17.7 \text{ }\mu\text{m}$, $\sigma_{x'} = 26.4 \text{ }\mu\text{rad}$, $\sigma_{z'} = 2.2 \text{ }\mu\text{rad}$). As the contribution of the energy spread is independent of the harmonic number, the effect of the energy spread on the lower order harmonics combines with the homogeneous linewidth, whereas for higher order harmonics the broadening is mainly determined by the energy spread. Given that the HU640 is composed of 14 periods, then $\left(\frac{\Delta\lambda}{\lambda}\right)_{hom} = 7\%$ for H1, and $\left(\frac{\Delta\lambda}{\lambda}\right)_{hom} = 2\%$ for H3.

Figure 12 compares the calculated flux density emitted by the U20 undulator operating in the high energy range considering the present SOLEIL horizontal emittance and energy spread and that modified due to the assumed presence of a RW. The flux density of the harmonic H1 is not affected and that of the harmonic H11 is reduced by about 18%. The different contributions to the total harmonic broadening are: $\left(\frac{\Delta\lambda}{\lambda}\right)_{\sigma_e} \approx 2.8 \times 10^{-3}$, $\left(\frac{\Delta\lambda}{\lambda}\right)_{\epsilon} = 9.14 \times 10^{-3}$ and $\left(\frac{\Delta\lambda}{\lambda}\right)_{\sigma} = 6.79 \times 10^{-3}$ (calculated at the source point: $\sigma_x = 265.1 \text{ }\mu\text{m}$, $\sigma_z = 9.5 \text{ }\mu\text{m}$, $\sigma_{x'} = 30.5 \text{ }\mu\text{rad}$, $\sigma_{z'} = 4.1 \text{ }\mu\text{rad}$). Concerning the harmonic H1, the homogeneous linewidth dominates the effects of the energy spread ($\left(\frac{\Delta\lambda}{\lambda}\right)_{hom} = 10^{-2}$, the

U20 is composed of 98 periods). Flux reduction noticed of the harmonic H11 is due to the combination between the energy spread and the homogeneous linewidth ($\left(\frac{\Delta\lambda}{\lambda}\right)_{hom} = 9 \times 10^{-3}$).

Increasing the energy spread has a greater effect on the harmonic intensity for the U20 undulator compared to the HU640 one due to larger contribution of the emittance and the energy spread to the inhomogeneous broadening in the case of the U20. In addition, the homogeneous broadening is larger for the HU640 than for the U20.

IV. CONCLUSION

The Robinson effect was observed and validated experimentally at SOLEIL. This novel development is a critical step forward achieved even without constructing a RW. The experiment was performed by making use of the high field and field gradient of already installed undulators in the storage. The expected Robinson effects on reducing the horizontal emittance and increasing the energy spread are observed in agreement with theoretical expectations: horizontal emittance is reduced by ratio of 35% and the energy spread is increased by ratio of 30% with respect to the present values. RW has an impact on the spectral distribution of the photon flux density emitted by insertion devices. In the low energy range it leads to a very tiny photon flux reduction, while in the high energy range it has a much larger effect on the photon flux. This makes a RW not a good candidate for synchrotron radiation facilities, but an excellent candidate for machines providing collision experiments which require beams of

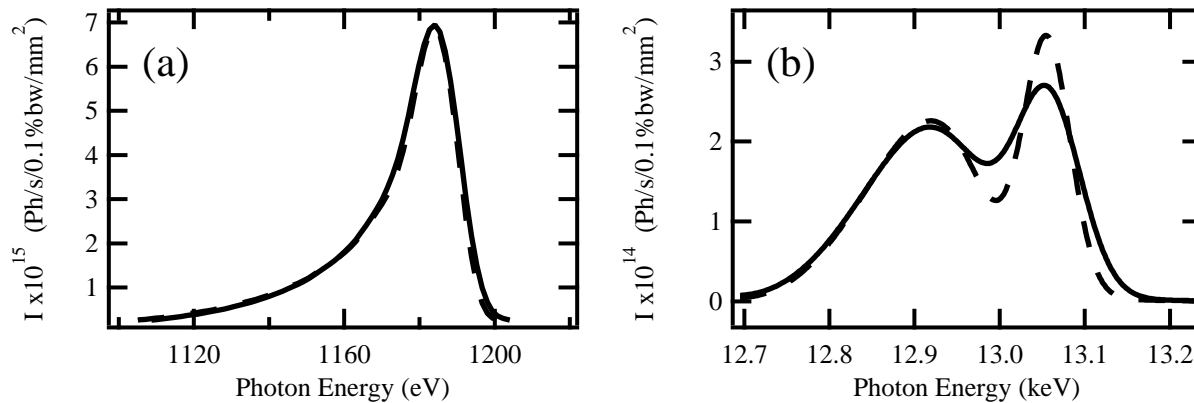


FIG. 12. Flux density emitted by the undulator U20 ($K = 2$) calculated with SRW through an aperture of $0.1 \times 0.1 \text{ mm}^2$ located at 10 m from the source. (a): zoom on the harmonic H1, (b) zoom on the harmonic H11. — $\epsilon_x = 1.95 \text{ nm.rad}$, $\sigma_e = 1.428 \times 10^{-3}$. - - $\epsilon_x = 3.9 \text{ nm.rad}$, $\sigma_e = 1.01 \times 10^{-3}$. The beam energy is 2.75 GeV, the beam current is 500 mA.

tiny dimensions.

manuscript and for giving his time for continuous and constructive discussions.

ACKNOWLEDGMENTS

The author would like to acknowledge Ryutaro Nagaoka from Synchrotron SOLEIL for reviewing this

-
- [1] B. Lengeler, *Naturwissenschaften* **88**, 249 (2001).
- [2] Z. Huang *et al.*, *Brightness and coherence of synchrotron radiation and FELs*, Tech. Rep. (SLAC National Accelerator Laboratory (SLAC), 2013).
- [3] J. Miao, P. Charalambous, J. Kirz, and D. Sayre, *Nature* **400**, 342 (1999).
- [4] A. Kondratenko and A. Skrinsky, *Optics and Spectroscopy* **42**, 189 (1977).
- [5] K.-J. Kim, *Nuclear Instruments and Methods in Physics Research Section A: Accelerators, Spectrometers, Detectors and Associated Equipment* **21**, 862 (2014).
- [6] S. Krinsky, *IEEE Transactions on Nuclear Science* **NS-30**, 3078 (1983).
- [7] T. Tanaka and H. Kitamura, *Journal of Synchrotron Radiation* **16**, 380 (2009).
- [8] A. Nadji, P. Brunelle, M.-E. Couprie, J.-C. Denard, J.-M. Filhol, J.-F. Lamarre, P. Lebasque, A. Loulergue, P. Marchand, R. Nagaoka, and M.-A. Tordeux, in *Proceedings of IPAC11* (San Sebastian, Spain, 2011) pp. 3002–3004.
- [9] R. Bartolini, in *Proceedings of PAC07* (New Mexico, USA, 2007) pp. 1109–1111.
- [10] M. Borland, *Journal of Physics: Conference Series*, **425**, 042016 (2013).
- [11] R. Hettel, *Journal of Synchrotron Radiation* **21**, 843 (2014).
- [12] S.-Y. Lee, *Accelerator Physics* (World Scientific Publishing Co Inc, 2004).
- [13] H. Wiedemann, *Nuclear Instruments and Methods in Physics Research Section A: Accelerators, Spectrometers, Detectors and Associated Equipment* **27**, 1 (2014).
- [14] E. Courant and H. Snyder, *Annals of Physics* **3**, 1 (1958).
- [15] J. Bengtsson, in *Proceedings of EPAC08, invited* (Genoa, Italy, 2008) pp. 988–992.
- [16] M. Berz, K. Makino, and W. Wan, *An introduction to beam physics* (Taylor and Francis, 2015) p. 230.
- [17] D. Einfeld, J. Schaper, and M. Plesko, in *Proceedings of PAC95* (Dallas, Texas, 1995) pp. 177–179.
- [18] S.-C. Leemann, A. Andersson, M. Eriksson, L.-J. Lindgren, E. Wallén, J. Bengtsson, and A. Streun, *Phys. Rev. ST Accel. Beams* **12**, 120701 (2009).
- [19] P.-F. Tavares, S.-C. Leemann, M. Sjöström, and A. Andersson, in *Proceedings of IPAC16* (Chicago, IL, USA, 2016) pp. 439–444.
- [20] M. Eriksson, L. Malmgren, E. Al-Dmour, S. Thorin, M. Johansson, S.-C. Leemann, A. Andersson, and P.-F. Tavares, in *proceeding of IPAC16* (Chicago, IL, USA, 2016) pp. 439–444.
- [21] K. Tsumaki and N. Kumagai, *Nuclear Instruments and Methods in Physics Research Section A: Accelerators, Spectrometers, Detectors and Associated Equipment* **565**, 394 (2006).
- [22] H. Tanaka, S. Goto, T. Ishikawa, S. Takano, T. Watanabe, and M. Yabashi, in *Proceedings of IPAC16* (Busan, Korea, 2016) pp. 2867–2870.
- [23] J.-C. Biasci, J.-F. Bouteille, N. Carmignani, J. Chavanne, D. Coulon, Y. Dabin, F. Ewald, L. Farvacque, L. Goirand, M. Hahn, J. Jacob, G. LeBec, S. Liuzzo, B. Nash, H. Pedroso-Marques, T. Perron, E. Plouviez, P. Raimondi, J.-L. Revol, K. Scheidt, and M. Sjöström, *Synchrotron Radiation News* **27**, 1 (2014), <https://doi.org/10.1080/08940886.2014.970931>.
- [24] P. Raimondi, in *Proceedings of IPAC16* (Busan, Korea, 2016) pp. 2023–2027.

- [25] M. Borland, *Exploration of a Tevatron-sized ultimate storage ring*, Tech. Rep. (Argonne National Laboratory (ANL), 2012).
- [26] P. Emma and T. Raubenheimer, *Phys. Rev. ST Accel. Beams* **4**, 021001 (2001).
- [27] M. Tischer, K. Balewski, W. Decking, M. Seidel, L. Yongjun, P. Vobly, V. Kuzminykh, K. Zolotariov, and E. Levichev, in *Proceedings of PAC 2005* (Knoxville, Tennessee, 2005) pp. 2446–2448.
- [28] W. Guo, S. Kramer, S. Krinsky, Y. Li, B. Nash, and T. Tanabe, in *Proceedings of PAC09* (Vancouver, BC, Canada, 2009) pp. 1102–1104.
- [29] Y. Nosochkov, K. Bane, Y. Cai, R. Hettel, and M.-H. Wang, in *Proceedings of IPAC11* (San Sebastian, Spain, 2011) pp. 3068–3070.
- [30] K. Robinson, *Physical Review* **111**, 373 (1958).
- [31] A. Hofmann, in *proceedings of ICHEA* (1967).
- [32] Y. Baconnier, R. Cappelletti, J.-P. Riinaud, H.-H. Umstätter, M.-P. Level, M. Sommer, and H. Zygier, *Nuclear Instruments and Methods in Physics Research Section A* **504**, 161 (2003).
- [33] J. Li, G. Liu, W. Xu, and W. Li, in *Proceedings of IPAC13* (Shanghai, China, 2013) pp. 2009–2011.
- [34] S.-Q. Tian, Q.-L. Zhang, M.-Z. Zhang, K. Wang, and B.-C. Jiang, *Nuclear Science and Techniques* **28**, 9 (2017).
- [35] T. Goetsch, J. Feikes, M. Ries, and G. Wüstefeld, in *Proc. IPAC14* (Dresden, Germany, 2014) pp. 2001–2003.
- [36] T. Tydecks, *A Robinson Wiggler for the Metrology Light Source*, Ph.D. thesis, Berlin University (2016).
- [37] H. Abualrob, P. Brunelle, M.-E. Couprie, O. Marcouillé, A. Nadji, L. Nadolski, and R. Nagaoka, in *Proceedings of IPAC12* (New Orleans, USA, 2012) pp. 702–704.
- [38] M. Sands, *The Physics of Electron Storage Rings. An Introduction* (SLAC-R-121, 1971).
- [39] C. Benabderrahmane, P. Berteaud, F. Briquez, P. Brunelle, O. Chubar, M.-E. Couprie, J.-M. Filhol, M. Girault, O. Marcouillé, F. Marteau, M. Massal, F. Paulin, M. Valleau, and J. Veteran, in *Proceedings of PAC07* (Albuquerque, New Mexico, USA, 2007) pp. 929–931.
- [40] M.-E. Couprie, C. Benabderrahmane, P. Berteaud, F. Briquez, L. Chapuis, O. Chubar, T. Elajjouri, F. Marteau, J.-M. Filhol, C. Kitegi, O. Marcouillé, M. Massala, M. Valleau, and J. Vétéran, in *Proceedings of AIP Conference*, Vol. 1234 (AIP, 2010) pp. 519–522.
- [41] P. Elleaume, O. Chubar, and J. Chavanne, in *Proceedings of PAC97* (Vancouver, Canada, 1997) pp. 3509–3511.
- [42] O. Chubar, P. Elleaume, and J. Chavanne, *Journal of Synchrotron Radiation* **5**, 481 (1998).
- [43] A. Terebilo, *Performance Issues at Synchrotron Light Sources*, Advanced Light Source, Lawrence Berkeley Lab, Berkeley, CA, USA (2001).
- [44] M.-A. Tordeux, L. Cassinari, O. Chubar, J.-C. Denard, D. Pédeau, and B. Pottin, in *Proceedings of DIPAC07* (Venice, Italy, 2007) pp. 180–182.
- [45] M. Labat, L. Cassinari, M.-E. Couprie, R. Nagaoka, and D. Pédeau, in *Proceedings of DIPAC07* (Venice, Italy, 2007) pp. 241–243.
- [46] O. Chubar and P. Elleaume, in *Proceedings of EPAC98* (Stockholm, Sweden, 1998) pp. 1177–1179.
- [47] <http://www.hamamatsu.com>.